J. Eur. Opt. Society-Rapid Publ. 2024, **20**, 5

https://doi.org/10.1051/jeos/2024003
Available online at: https://jeos.edpsciences.org

EOSAM 2023
Guest editors: Patricia Segonds, Guy Millot and Bertrand Kibler

Journal of the European Optical Society-Rapid Publications

RESEARCH ARTICLE

OPEN ACCESS

Mueller matrix imaging polarimeter with polarization camera self-calibration applied to structured light components

Esther Nabadda[1], María del Mar Sánchez-López[1,2,*], Asticio Vargas[3], Angel Lizana[4], Juan Campos[4], and Ignacio Moreno[1,5]

[1] Instituto de Bioingeniería, Universidad Miguel Hernández de Elche, 03202 Elche, Spain
[2] Departamento de Física Aplicada, Universidad Miguel Hernández de Elche, 03202 Elche, Spain
[3] Departamento de Ciencias Físicas, Universidad de La Frontera, Temuco, Chile
[4] Departament de Física, Universitat Autònoma de Barcelona, 08193 Bellaterra, Barcelona, Spain
[5] Departamento de Ciencia de Materiales, Óptica y Tecnología Electrónica, Universidad Miguel Hernández de Elche, 03202 Elche, Spain

Received 8 August 2023 / Accepted 25 January 2024

Abstract. This work presents a complete Mueller matrix imaging polarimeter that uses three liquid-crystal retarders and a pixelated polarization camera. The polarimeter is characterized and optimized with a standard correction procedure here adapted to be performed fully in-situ, without any additional element, based on considering the polarization camera as the reference. The accuracy limit caused by the extinction ratio in the camera micro-polarizers is analyzed. Finally, the imaging polarimeter is tested experimentally by analyzing well-known samples for structured light applications such as patterned retarders, a patterned polarizer, and a liquid-crystal depolarizer. The work is presented in a tutorial style useful to reproduce the procedure by non-experts in polarimetry.

Keywords: Polarimetry, Liquid-Crystals Retarders, Structured Light, Polarization Camera.

1 Introduction

Among the different properties of light, polarization has been demonstrated to provide extremely useful information [1]. This is becoming especially relevant in bioimaging, where several techniques harnessing biological and clinical research are based on the vectorial properties of light [2, 3]. In the last decades, important technological advances related to the generation and measurement of polarized light have been produced, that provide tools and devices like liquid-crystal variable retarders, spatial light modulators (SLM) or polarization cameras that have become common in optics laboratories, leading to the development of precise imaging polarimeters [4, 5].

Another field developed in parallel is the generation and detection of structured light. This denomination was introduced to describe light beams with a spatial and temporal control of their amplitude, phase and state of polarization [6]. Light beams with non-uniform polarization, known as vector beams, are prompting important advances in areas such as microscopy, materials processing, metrology, or optical communications [7, 8]. Structured light is typically produced with patterned polarization elements [9, 10]. SLM devices show the advantage of being reconfigurable, although requiring bulk optical systems [11, 12]. Alternatively, flat patterned polarization components can be fabricated with metamaterials [13] or with liquid-crystal (LC) geometric-phase elements [14, 15]. Patterned polarizers with arbitrary spatial distributions of the transmission axis are of great interest especially for developing micro-polarizers in polarization cameras [16].

Research in patterned polarization elements and research in polarimetric imaging are closely related [17]. While patterned polarization elements are providing new tools for advanced polarization imaging [18, 19], polarimetric imaging relying on the Mueller matrix has proven very worthy to evaluate the quality of the fabricated components [20, 21]. Although Mueller matrix imaging polarimetry has been employed for almost three decades [22], it is a technique in constant evolution, where multiple variants have been introduced over the years [23, 24]. In this context, this work presents the realization of a complete Mueller matrix (MM) imaging polarimeter whose performance is tested on polarization elements commonly applied to generate structured light. This polarimeter is based on our previous system [21], but here we provide the following

* Corresponding author: mar.sanchez@umh.es

improvements: (1) the use of a multiwavelength LED light source to avoid interference and speckle noise, (2) the realization of a setup on a rotatable breadboard to easily change the polarimeter from a transmission to a back-reflection configuration, (3) the use of spectrally calibrated liquid-crystal retarders (LCR), both in the polarization state generator (PSG) and in the polarization state analyzer (PSA), and (4) the application of a well-stablished sequential polarimeter calibration and optimization method [25], here adapted to consider the polarization camera as the reference for polarization measurements (self-calibration). This way, the method can be applied without any additional elements simply by properly tuning the LCR devices in the system. These improvements allow us to present a multifunctional complete MM imaging polarimeter that can be applied to a variety of samples.

The paper is organized as follows: after this introduction, Section 2 describes the polarimeter components. Then, Section 3 presents the calibration steps required to correctly operate the system, including the correct tuning of the LCR devices and the calibration and compensation procedure of the PSG and the PSA systems. Finally, in Section 4 we discuss the results obtained to evaluate different elements used in structured light like spatially patterned retarders and polarizers, and a liquid-crystal depolarizer.

2 Description of the imaging polarimeter

The developed imaging polarimeter system is shown in Figure 1. As mentioned, it represents an upgraded version of our previous system [21] with larger potential for sample imaging and quality control applications. The light source is a multiwavelength RGB LED (Thorlabs LED4D067) with controllable intensity level. A light guide (Thorlabs LLG05-4H) directs the light to the polarimeter entrance. A 50 mm photographic objective lens is used to image the lightguide output onto the sample. A diffuser (Edmund Holo 30 deg) is added to improve the intensity uniformity on the sample plane. The PSG is composed by a vertically oriented linear polarizer, and two liquid-crystal variable retarders (LCR1 and LCR2) from ARCOptix. LCR1 is oriented at 45° while LCR2 is oriented vertically, such that upon adjusting their retardances, an arbitrary fully-polarized state of polarization (SOP) can be generated.

The polarized light illuminates the sample and after light-matter interaction the output is analyzed with a PSA. A circular iris diaphragm of variable diameter is placed just in front of the sample plane and kept in the calibration procedure. The PSA is an imaging detector that comprises a polarization camera and another variable retarder (LCR3), also from ARCOptix. The sample and the PSA are positioned on a rotating breadboard (Thorlabs RBB300A/M), so the detection system can be rotated an angle θ, changing from a transmission configuration (Fig. 1e) to a reflection configuration (Fig. 1f). The transmission configuration is used in the calibration process, and it is useful for analyzing highly transparent samples. The reflection configuration is suitable for samples with high scattering and for reflective devices.

The polarization camera (Thorlabs CS505MUP Kiralux) is a monochrome sensor with 12 bit resolution (4096 intensity digital levels) and with 2448 × 2048 square pixels of 3.45 µm side. The sensor includes an integrated micro-polarizer array attached to the pixel detectors. Thus, images for horizontal (H), vertical (V), diagonal (D) and antidiagonal (A) linear analyzers can be captured in a single shot (Fig. 1c). An objective macro zoom lens (Computar MLH 10X) is attached to the polarization camera; thus, the sample can be imaged with relatively large magnification at distances around 20 cm. If larger magnification is required, an extension tube is added.

The three RGB LEDs of the light source have central wavelengths at 660 nm (red light), 565 nm (green light) and 470 nm (blue light) respectively. Figure 1d shows the spectra of the three LEDs, measured with a spectrometer (Stellar-Net, STN-BLK-C-SR) in the spectral range from 400 to 700 nm, with 2 nm resolution). A spectral filter (SF) filters each of these LED spectra, resulting in filtered spectra with full width at half maximum (FWHM) of about 10 nm, as the measured narrow RGB bands shown in Figure 1d. The SF is useful to reduce depolarization values that might have been artificially added to the final measurements due to the LCRs wavelength retardance dependence.

3 Calibration procedure

This section presents the calibration procedures required to accurately operate the MM imaging polarimeter. First, we review the method for calibrating the LCR devices. Then, the following subsection describes the calibration and optimization of the polarimeter.

3.1 Calibration of the LCR devices

The first step to properly operate the polarimeter is to calibrate the retardance of the LCR devices that will be used to provide the required SOPs, both in the PSG and in the PSA. For that purpose, we follow a simple yet accurate enough procedure that consists in placing the LCR device between crossed/parallel polarizers, oriented at 45° with respect to the LC director axis [26, 27]. The normalized transmission for crossed polarizers is given by

$$T_{\perp}(\lambda,\ V) = \cos^2\left[\frac{1}{2}\varphi(\lambda,\ V)\right], \tag{1}$$

where the LC retardance $\varphi(\lambda,\ V) = (2\pi/\lambda)\cdot\Delta n\cdot t$ depends on the thickness of the LC layer (t), $\Delta n(V)$ is the voltage-dependent birefringence, λ is the wavelength and V is the applied voltage. This relation shows the expected oscillatory behavior of $T_{\perp}$ (λ, V) both as a function of λ and V.

We measured the LCRs retardance versus the applied voltage for the three wavelength bands. As an example, Figure 2 shows the results obtained for LCR1. Figure 2a illustrates the normalized transmission curves $T_{\perp}$ (V) for the three wavelength bands centered at λ_{R} = 660 nm,

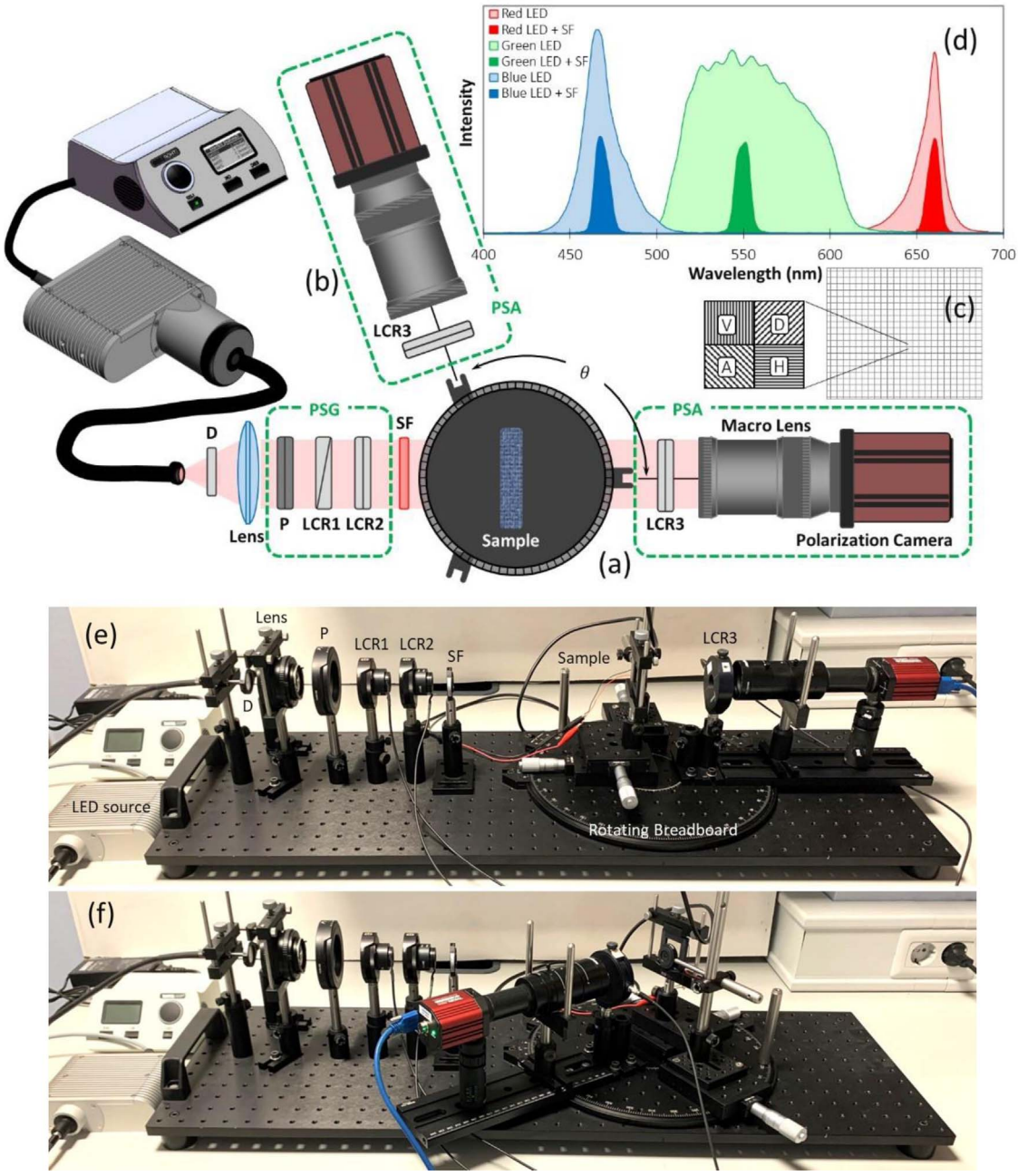

Fig. 1. Scheme of the Mueller matrix imaging polarimeter. D: diffuser. SF: Spectral filter. P: linear polarizer. LCR: liquid-crystal retarders. (a) Transmission geometry. (b) Reflection geometry. (c) Scheme of the micro-polarizers pattern on a macro-pixel of the polarization camera. (d) Spectra of the three LED sources with central wavelengths of 470 nm, 565 nm and 660 nm, and after being filtered by the corresponding spectral filter (SF). Pictures of the system in (e) the transmission configuration and (f) the reflection configuration.

$\lambda_G = 565$ nm and $\lambda_B = 470$ nm. The curves feature the typical oscillatory behavior, with more oscillations for the shortest blue wavelength. Figure 2b shows the retrieved retardance function $\varphi(V)$ for the three wavelengths. For the longer wavelength $\lambda_R = 660$ nm the retardance variation is slightly greater than 2π, while it almost reaches 3π and 3.5π for the green and blue bands respectively.

3.2 Calibration of the PSG

We operate the polarimeter to generate and detect the well-known polarimetric basis consisting of six standard SOP: namely horizontal (H), vertical (V), diagonal (D) and antidiagonal (A) linear states, and right (R) and left (L) circular states. These six SOP define an octahedron in the

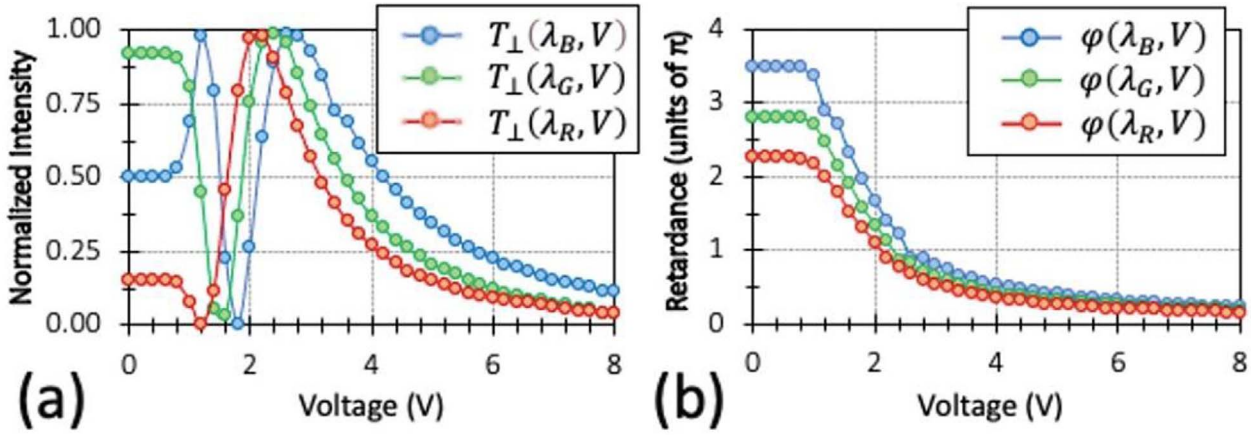

Fig. 2. Example of calibration of an LCR device in the MM imaging polarimeter. (a) Transmission $T_\perp(V)$ between crossed polarizers oriented at 45° with respect to the LC director. (b) LCR retardance $\varphi(V)$. Both graphs show the results for the three bands, with central wavelengths 470 nm (B), 565 nm (G) and 660 nm (R).

Table 1. Retardances required on LCR1 and LCR2 to provide SOP in the PSG.

SOP generated with PSG	H	V	D	A	R	L
LCR1 Retardance	HW	FW	QW	QW	QW	3QW
LCR2 Retardance	FW	FW	QW	3QW	FW	FW

QW: quarter-wave; HW: half-wave; 3QW: three quarter-wave; FW: full-wave.

Poincaré sphere and provide the polarimeter ideal conditional number (CN = 1.732) [25], thus ensuring an optimal performance in terms of noise amplification minimization from intensity measurements to polarimetric measurements. The LCR calibration provides the required voltages; typically, the quarter-wave retardance, the half-wave retardance or the full-wave retardance. Considering that the PSG polarizer (P) is oriented vertically, LCR1 is at 45° and LCR2 is vertical, Table 1 provides the retardances required to achieve the input SOPs.

However, variable LCRs feature effects that might introduce inaccuracy in the polarimeter, being the most relevant the non-uniform retardance on the clear aperture [26], the retardance temperature dependance, and multiple reflection interference effects that cause intensity variations coupled to the retardance modulation [28]. These effects must be compensated to achieve accurate polarimetric values. Among the different methods [29–31], here we propose and apply a modification of a well-stablished sequential calibration and optimization method [32, 33]. In the typical procedure, a calibrated polarimeter serves as the reference to measure the SOP of the PSG states, and the results are compared to those measured with the developed polarimeter. Here the technique is adapted to consider the polarization camera as the reference. This way, a self-reference procedure is applied that does not require any additional external element. Of course, the accuracy of this self-calibration depends on the quality of the micro-polarizers in the polarization camera. To this goal Appendix A includes an analysis of the limits of this procedure considering the extinction ratio of the micro-polarizers in the camera. We measured extinction ratios over 120:1. Although other sources of error have been identified [34] (such as spatial variations of the extinction ratio or misalignments in the orientation of the micro-polarizers), here we assume this simplified model with a limited but uniform extinction ratio. According to the approach described in the Appendix, the self-calibration procedure leads to an error in the measured MM elements below 1.7%.

Figure 3 shows the intensity captured for the circular iris diaphragm under red light illumination. The polarization camera provides a four-quadrant image where quadrants i, ii, iii and iv correspond to the detection of the V, D, A and H linear states. The input intensity is adjusted to ensure the non-saturation of the camera and it is maintained in the sample characterization. Each picture in Figure 3 corresponds to one of the six standard input SOP generated with the PSG (H, V, D, A, R, L). In each case, the voltage values derived from the LCR1 and LCR2 calibrations are taken as the starting point, but a fine adjustment must be then performed to provide images like those in Figure 3. The successful generation of the linear states H, V, A and D is verified when the following conditions are simultaneously fulfilled: the image quadrant of the orthogonal detector becomes the darkest, the image quadrant corresponding to the given input state is the brightest, and the other two quadrants feature the same intensity. On the contrary, the generation of the circular R and L states is verified when the four quadrants appear with equal weight. The information provided by the LCR calibration in Figure 2 allows differentiating

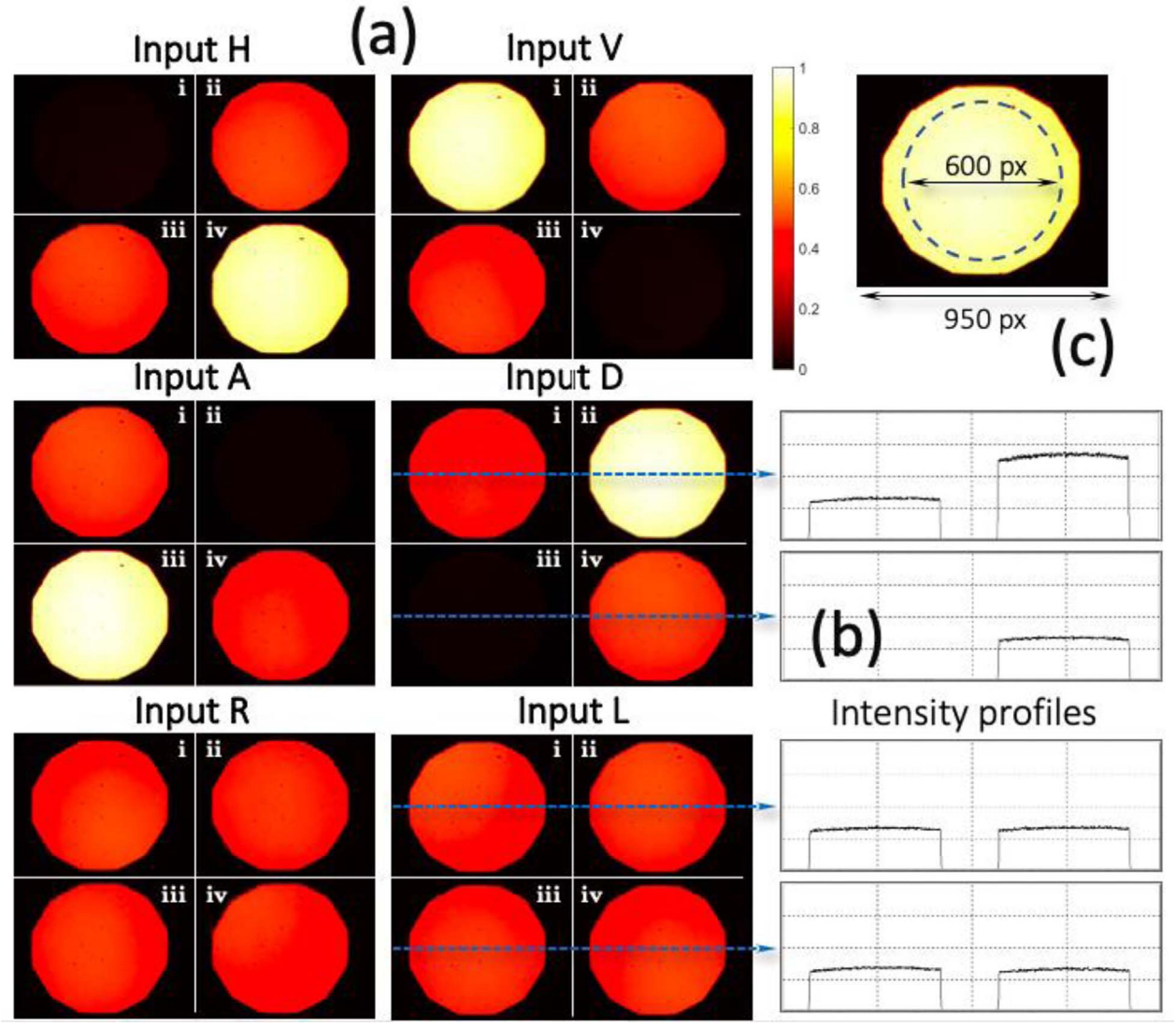

Fig. 3. (a) Calibration of the PSG system: experimental four-quadrant images captured by the polarization camera under the red channel illumination for input SOPs as linear horizontal (H), vertical (V), antidiagonal (A), diagonal (D), circular left (R) and circular right (L). (b) The intensity profiles for inputs D and L. (c) Calculations of average values are performed in the central circle with diameter of 600 pixels.

R and L states. On the right, the intensity profiles of the four quadrants for inputs D and L are shown.

The polarization camera is an incomplete polarimeter, since only the linear polarization components are measured. The first three Stokes parameters S_0, S_1, S_2 can be retrieved from the intensity images $I_i(x, y)$, $I_{ii}(x, y)$, $I_{iii}(x, y)$, and $I_{iv}(x, y)$ captured in quadrants *i*, *ii*, *iii*, and *iv* as

$$S_0(x,y) = \frac{1}{2}[I_i(x,y) + I_{ii}(x,y) + I_{iii}(x,y) + I_{iv}(x,y)], \quad (2a)$$

$$S_1(x,y) = I_{iv}(x,y) - I_i(x,y), \quad (2b)$$

$$S_2(x,y) = I_{ii}(x,y) - I_{iii}(x,y). \quad (2c)$$

To retrieve S_3, a quarter-wave plate must be placed in front of the polarization camera, to measure the circular polarization components. However, since LCR2 is oriented vertical, a quarter-wave retardance can be added to this retarder to achieve an equivalent situation and make quadrants *ii* and *iii* behave as equivalent R and L circular analyzers. Therefore, the PSG calibration can be completed with

$$S_3(x,y) = I'_{ii}(x,y) - I'_{iii}(x,y), \quad (2d)$$

where now I' indicates that the additional quarter-wave retardance is added to LCR2. Note that LCR1 and LCR2 devices remain within the PSG system in all measurements, and they simply change voltage, so there are not differences due to reflection or absorption losses.

Table 2. Average intensity values and standard deviation of the images shown in Figure 3.

Input H		Input V	
$\langle I_i \rangle = 0.014 \pm 0.002$	$\langle I_{ii} \rangle = 0.496 \pm 0.013$	$\langle I_i \rangle = 0.938 \pm 0.021$	$\langle I_{ii} \rangle = 0.498 \pm 0.013$
$\langle I_{iii} \rangle = 0.493 \pm 0.012$	$\langle I_{iv} \rangle = 0.923 \pm 0.021$	$\langle I_{iii} \rangle = 0.494 \pm 0.014$	$\langle I_{iv} \rangle = 0.017 \pm 0.002$
Input A		Input D	
$\langle I_i \rangle = 0.497 \pm 0.012$	$\langle I_{ii} \rangle = 0.016 \pm 0.002$	$\langle I_i \rangle = 0.448 \pm 0.012$	$\langle I_{ii} \rangle = 0.954 \pm 0.021$
$\langle I_{iii} \rangle = 0.957 \pm 0.021$	$\langle I_{iv} \rangle = 0.490 \pm 0.013$	$\langle I_{iii} \rangle = 0.018 \pm 0.002$	$\langle I_{iv} \rangle = 0.504 \pm 0.013$
Input R		Input L	
$\langle I_i \rangle = 0.501 \pm 0.024$	$\langle I_{ii} \rangle = 0.501 \pm 0.017$	$\langle I_i \rangle = 0.497 \pm 0.020$	$\langle I_{ii} \rangle = 0.511 \pm 0.014$
$\langle I_{iii} \rangle = 0.495 \pm 0.015$	$\langle I_{iv} \rangle = 0.496 \pm 0.022$	$\langle I_{iii} \rangle = 0.508 \pm 0.014$	$\langle I_{iv} \rangle = 0.523 \pm 0.023$

Table 2 presents the average value of the intensity measured for each of the 6 × 4 images shown in Figure 3. The error is given by the standard deviation. These values are calculated in a circle centered on the image and with diameter 600 pixels, as indicated in Figure 3c. These error values are also affected by noise in the detector. The camera was calibrated following a standard procedure [35] and it was operated in the regime limited by shot noise. The impact of this noise can be reduced by averaging several captures of each image, at the cost of increasing the time required for acquisition. Since we are using relatively high levels of intensity and samples with high transmission, we take single captures.

The measurement of the Stokes parameters for each PSG input state defines the **S** matrix, whose columns are given by images S_{ig} where index $i = 0, 1, 2, 3$ indicates the Stokes parameter, and index g denotes the state generated by the PSG (in our case. g = H, V, D, A, R, L). Thus, **S** is a 4 × 6 matrix defined as:

$$\mathbf{S} = \begin{pmatrix} S_{0H} & S_{0V} & S_{0D} & S_{0A} & S_{0R} & S_{0L} \\ S_{1H} & S_{1V} & S_{1D} & S_{1A} & S_{1R} & S_{1L} \\ S_{2H} & S_{2V} & S_{2D} & S_{2A} & S_{2R} & S_{2L} \\ S_{3H} & S_{3V} & S_{3D} & S_{3A} & S_{3R} & S_{3L} \end{pmatrix}$$

$$= \begin{pmatrix} 1 & 1 & 1 & 1 & 1 & 1 \\ 1 & -1 & 0 & 0 & 0 & 0 \\ 0 & 0 & 1 & -1 & 0 & 0 \\ 0 & 0 & 0 & 0 & 1 & -1 \end{pmatrix}, \quad (3)$$

where the second part of equation (3) denotes the ideal values. Since **S** is not a square matrix, its pseudo-inverse matrix is a 6 × 4 matrix given by:

$$\mathbf{S}^{-1} = \mathbf{S}^T \left[\mathbf{S} \cdot \mathbf{S}^T\right]^{-1} = \begin{pmatrix} 1/6 & 1/2 & 0 & 0 \\ 1/6 & -1/2 & 0 & 0 \\ 1/6 & 0 & 1/2 & 0 \\ 1/6 & 0 & -1/2 & 0 \\ 1/6 & 0 & 0 & 1/2 \\ 1/6 & 0 & 0 & -1/2 \end{pmatrix}, \quad (4)$$

where superindex T indicates the transposed matrix and where the matrix on the right corresponds again to the ideal values. This expression of the pseudo-inverse matrix is valid when it is considered to multiply a matrix on the right.

Figure 4 shows matrices $\mathbf{S}(x,y)$ and $\mathbf{S^{-1}}(x,y)$ retrieved from the data in Figure 3. We use a color map to represent values from +1 to −1. To avoid presenting calculations in pixels where the input light is blocked by the iris diaphragm, we calculated the average $I_{\text{mean}}(x, y)$ of the 24 images in Figure 3a and searched for its maximum value $M = \max[I_{\text{mean}}(x, y)]$. Then, polarimetric matrices and parameters are calculated at pixels (x, y) where $I_{\text{mean}}(x, y) > 0.2M$, while pixels not fulfilling this threshold are represented in black. The value 0.2 was tested to provide a visualization of the polarimetric parameters within the iris aperture, while the outside region, which otherwise would appear with random values, appears pitch black. The average values of each element in matrices $\mathbf{S}(x, y)$ and $\mathbf{S^{-1}}(x, y)$ were also calculated, together with its corresponding standard deviation, again within the circle defined in Figure 3c, leading to the results indicated in Table 3. These numerical results agree well with the expected theoretical values in equations (3) and (4).

3.3 Calibration of the PSA

Once the PSG has been calibrated, the polarimeter calibration is completed by adding the variable retarder LCR3 to the PSA and measuring again for each input SOP generated with the PSG. LCR3 is set with its axes oriented at 45°. LCR3 retardance is switched between zero or full-wave retardance, where the polarization camera measures H, V, D and A states, and a quarter-wave retardance, where circular R and L states can be measured at the micropixels with vertical and horizontal polarizers. This way, the PSA operates within an octahedron and it thus corresponds to the optimal solution named "T" in [36].

Setting the PSA to detect different SOPs yields the intensity matrix **I** defined by the images $I_{ag}(x, y)$, where a denotes the analyzer in the PSA and g denotes the input state at the PSG. We also select the six standard SOP for the PSA. Hence, **I** is a 6 × 6 matrix where each element I_{ag} is the intensity measured for each input state g = H, V, D, A, R, L when being detected through analyzer a = H, V, D, A, R, L, i.e.:

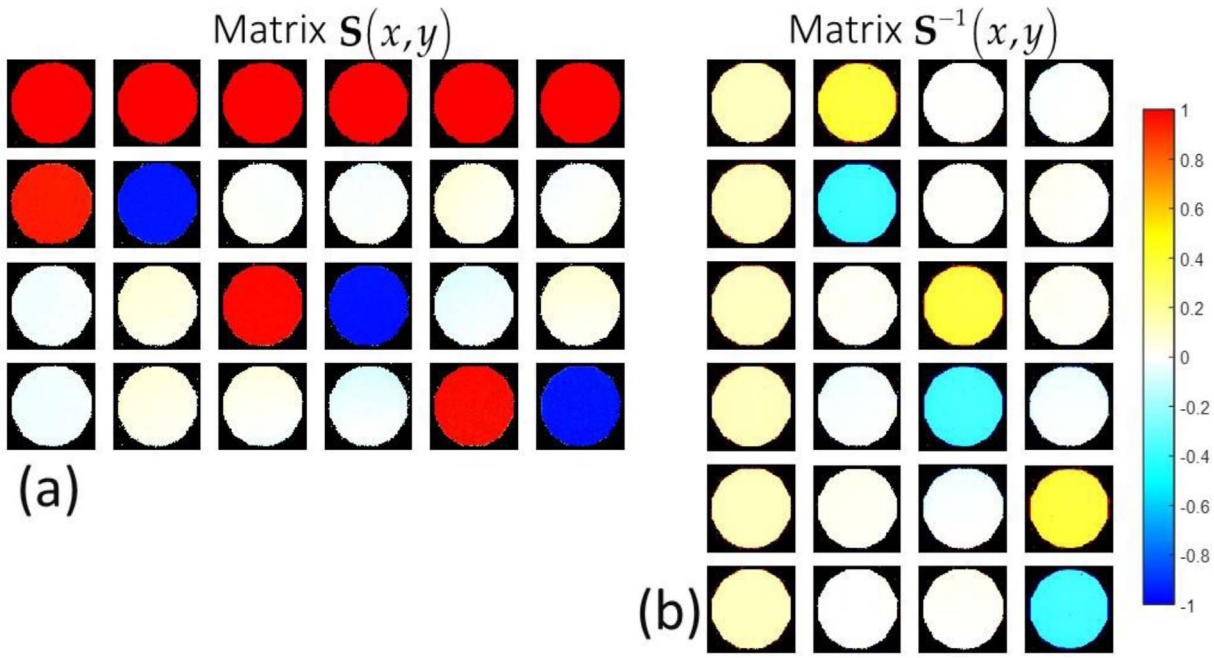

Fig. 4. Experimental images for the PSG polarimeter calibration under the red channel illumination. (a) $\mathbf{S}(x, y)$ matrix and (b) its pseudo-inverse matrix $\mathbf{S}^{-1}(x, y)$.

Table 3a. Average values of the matrix $\langle \mathbf{S}(x, y) \rangle_{\text{exp}}$.

1	1	1	1	1	1
+0.948±0.010	−0.960±0.010	−0.005±0.014	−0.015±0.014	+0.038±0.018	+0.006±0.016
−0.023±0.014	+0.034±0.016	+0.996±0.010	−0.965±0.010	−0.061±0.017	+0.075±0.020
+0.030±0.014	+0.025±0.017	+0.044±0.020	−0.057±0.022	+0.978±0.017	−0.962±0.017

$$\mathbf{I} = \begin{pmatrix} I_{HH} & I_{HV} & I_{HD} & I_{HA} & I_{HL} \\ I_{VH} & I_{VV} & I_{VD} & I_{VA} & I_{VL} \\ I_{DH} & I_{DV} & I_{DD} & I_{VA} & I_{DL} \\ I_{AH} & I_{AV} & I_{AD} & I_{AA} & I_{AL} \\ I_{RH} & I_{RV} & I_{RD} & I_{RA} & I_{RL} \\ I_{LH} & I_{LV} & I_{LD} & I_{LA} & I_{LL} \end{pmatrix}$$

$$= \begin{pmatrix} 1 & 0 & 1/2 & 1/2 & 1/2 & 1/2 \\ 0 & 1 & 1/2 & 1/2 & 1/2 & 1/2 \\ 1/2 & 1/2 & 1 & 0 & 1/2 & 1/2 \\ 1/2 & 1/2 & 0 & 1 & 1/2 & 1/2 \\ 1/2 & 1/2 & 1/2 & 1/2 & 1 & 0 \\ 1/2 & 1/2 & 1/2 & 1/2 & 0 & 1 \end{pmatrix}, \qquad (5)$$

where again the matrix values on the right stand for the ideal case.

Let us emphasize that matrix $\mathbf{I}$ is formed by images so each element $I_{ag}(x, y)$ depends on the pixel location. Also, note that the polarization camera only requires two shots to capture the six images per input SOP. Thus the 36 images required in matrix $\mathbf{I}$ are acquired after only 12 shots corresponding to 6 PSG configurations by 2 PSA configurations. Figure 5a shows the experimental result obtained for $\mathbf{I}(x, y)$ under the red channel illumination. For each input SOP, the images were normalized to the image where the analyzer matches the input polarization. The results bear good agreement with the ideal values in equation (6) despite slight variations along the diaphragm aperture. These variations are due to lighting non-uniformities (as shown in the intensity profiles in Fig. 3b), but also to the insertion of the LCR3 device in the PSA. Again, we calculated the average values and standard deviation of the intensity images in Figure 5a characterizing the intensity matrix. The result given in Table 4, although approximates reasonably well the expected values indicated in equation (5), shows significant differences that suggest the necessity of performing the compensation procedure to achieve accurate results.

Matrices $\mathbf{I}$ in equation (5) and $\mathbf{S}$ in equation (3) are related as $\mathbf{I} = \mathbf{A} \cdot \mathbf{S}$, where for simplicity we omit the pixel dependence. Here $\mathbf{A}$ is the detector matrix that characterizes the PSA. For the selected SOP, $\mathbf{A}$ is a 6×4 matrix that can be calculated as:

Table 3b. Average values of the matrix $\langle \mathbf{S}^{-1}(x,\ y)\rangle_{\text{exp.}}$

+0.159 ± 0.004	+0.497 ± 0.009	−0.004 ± 0.006	−0.009 ± 0.007
+0.159 ± 0.004	−0.504 ± 0.009	0.000 ± 0.006	+0.008 ± 0.007
+0.156 ± 0.004	+0.012 ± 0.006	+0.487 ± 0.009	+0.031 ± 0.007
+0.164 ± 0.004	−0.020 ± 0.007	−0.484 ± 0.009	−0.036 ± 0.008
+0.160 ± 0.004	+0.026 ± 0.007	−0.026 ± 0.008	+0.495 ± 0.009
+0.158 ± 0.004	0.000 ± 0.007	+0.024 ± 0.008	−0.487 ± 0.009

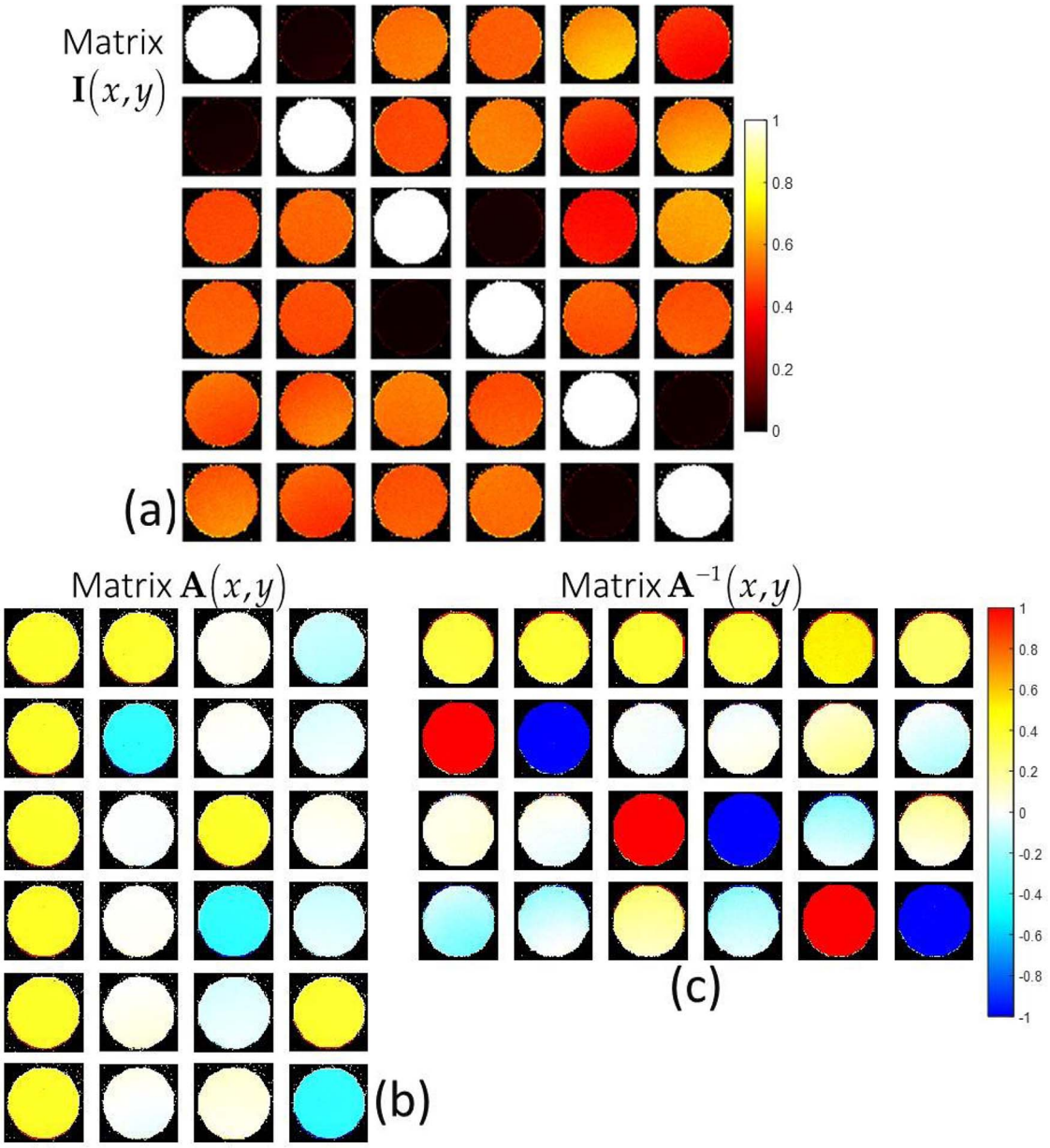

Fig. 5. Experimental images for the polarimeter PSA calibration under the red channel illumination. (a) Intensity matrix $\mathbf{I}(x,\ y)$. (b) Detector matrix $\mathbf{A}(x,\ y)$. (c) Pseudo-inverse detector matrix $\mathbf{A}^{-1}(x,\ y)$.

Table 4. Average values of the matrix $\langle \mathbf{I}(x,\, y)\rangle_{\text{exp}}$.

1	0.023 ± 0.004	0.544 ± 0.015	0.499 ± 0.014	0.395 ± 0.018	0.628 ± 0.025
0.035 ± 0.006	1	0.512 ± 0.017	0.537 ± 0.014	0.410 ± 0.020	0.617 ± 0.025
0.461 ± 0.012	0.527 ± 0.014	1	0.018 ± 0.002	0.498 ± 0.018	0.490 ± 0.017
0.532 ± 0.014	0.475 ± 0.013	0.029 ± 0.003	1	0.426 ± 0.016	0.581 ± 0.018
0.497 ± 0.022	0.525 ± 0.023	0.464 ± 0.014	0.579 ± 0.016	1	0.023 ± 0.002
0.541 ± 0.024	0.473 ± 0.023	0.580 ± 0.017	0.456 ± 0.014	0.023 ± 0.002	1

Table 5a. Average values of the matrix $\langle \mathbf{A}(x,\, y)\rangle_{\text{exp}}$.

+0.393 ± 0.008	+0.393 ± 0.010	+0.019 ± 0.008	−0.096 ± 0.012
+0.398 ± 0.009	−0.389 ± 0.012	−0.005 ± 0.011	−0.075 ± 0.013
+0.395 ± 0.009	−0.011 ± 0.008	+0.398 ± 0.011	+0.032 ± 0.015
+0.403 ± 0.008	+0.013 ± 0.008	−0.387 ± 0.011	−0.090 ± 0.015
+0.398 ± 0.008	0.001 ± 0.016	−0.066 ± 0.012	+0.384 ± 0.010
+0.398 ± 0.008	+0.022 ± 0.016	+0.068 ± 0.014	−0.387 ± 0.011

Table 5b. Average values of the matrix $\langle \mathbf{A}^{-1}(x,\, y)\rangle_{\text{exp.}}$

+0.39 ± 0.02	−0.41 ± 0.02	+0.43 ± 0.02	+0.42 ± 0.02	+0.55 ± 0.02	+0.310 ± 0.013
+0.96 ± 0.03	−0.99 ± 0.03	−0.04 ± 0.02	+0.02 ± 0.03	+0.07 ± 0.04	0.00 ± 0.04
+0.04 ± 0.02	−0.02 ± 0.03	+0.94 ± 0.03	−0.93 ± 0.03	−0.20 ± 0.05	+0.19 ± 0.05
−0.11 ± 0.05	−0.19 ± 0.05	+0.24 ± 0.04	−0.18 ± 0.04	+0.95 ± 0.03	−0.91 ± 0.03

$$\mathbf{A} = \mathbf{I}\cdot\ \mathbf{S}^{-1} = \begin{pmatrix} 1/2 & 1/2 & 0 & 0 \\ 1/2 & -1/2 & 0 & 0 \\ 1/2 & 0 & 1/2 & 0 \\ 1/2 & 0 & -1/2 & 0 \\ 1/2 & 0 & 0 & 1/2 \\ 1/2 & 0 & 0 & -1/2 \end{pmatrix}, \tag{6}$$

where the pseudo-inverse matrix $\mathbf{S}^{-1}$ in equation (4) was applied. The corresponding pseudo-inverse matrix $\mathbf{A}^{-1}$ is a 4×6 matrix given by

$$\mathbf{A}^{-1} = \left[\mathbf{A}^T\cdot\mathbf{A}\right]^{-1}\cdot\mathbf{A}^T$$
$$= \begin{pmatrix} 1/3 & 1/3 & 1/3 & 1/3 & 1/3 & 1/3 \\ 1 & -1 & 0 & 0 & 0 & 0 \\ 0 & 0 & 1 & -1 & 0 & 0 \\ 0 & 0 & 0 & 0 & 1 & -1 \end{pmatrix}, \tag{7}$$

where the matrices on the right in equations (6) and (7) correspond to the ideal values. This expression in equation (7) is valid when it is considered to multiply a matrix on the left.

Figures 5b and 5c show the experimental images of $\mathbf{A}(x,\, y)$ and $\mathbf{A}^{-1}(x,\, y)$, which again bear a good agreement with the expected values in equations (6) and (7). However, note some elements of $\mathbf{A}^{-1}$ in Figure 5c appreciably differ from the ideal zero value in equation (7), indicating the correction that the PSA experimental matrix requires. Let us remark that these matrices are calculated at every pixel, thus providing a PSA calibration at pixel level. Again, for each element on these matrices, we calculated the average value and its standard deviation on the circle defined in Figure 3c. The results are given in Table 5. These values differ appreciably from the ideal values in equations (6) and (7) since they account for the non-ideal behaviour of the components involved in the PSG and the PSA.

4 Mueller matrix imaging

Once the PSG and PSA matrices, $\mathbf{S}(x,\, y)$ and $\mathbf{A}(x,\, y)$, have been determined, the sample can be introduced in the polarimeter. For each input SOP generated by the PSG, the images given by the PSA are captured. As a result, a new set of 36 images are obtained that define a new intensity matrix $\mathbf{I}_{\text{S}}(x,\, y)$, like in equation (5), now related to the sample Mueller matrix $\mathbf{M}_{\text{S}}(x,\, y)$ as

$$\mathbf{I}_{\text{S}}(x, y) = \mathbf{A}(x, y)\cdot\mathbf{M}_{\text{S}}(x, y)\cdot\mathbf{S}(x, y). \tag{8}$$

$\mathbf{M}_{\text{S}}(x,\, y)$ is then obtained with the aid of the pseudo-inverse matrices $\mathbf{A}^{-1}$ and $\mathbf{S}^{-1}$ as:

$$\mathbf{M}_{\text{S}}(x, y) = \mathbf{A}^{-1}\cdot\mathbf{I}_{\text{S}}\cdot\mathbf{S}^{-1}$$
$$= \left\{\left[\mathbf{A}^T\cdot\mathbf{A}\right]^{-1}\cdot\mathbf{A}^T\right\}\cdot\mathbf{I}_{\text{S}}\cdot\left\{\mathbf{S}^T\cdot\left[\mathbf{S}\cdot\mathbf{S}^T\right]^{-1}\right\}. \tag{9}$$

We illustrate the procedure by considering different polarization devices that modify the input SOP by three distinct physical mechanisms: a pure retarder, a pure diattenuator,

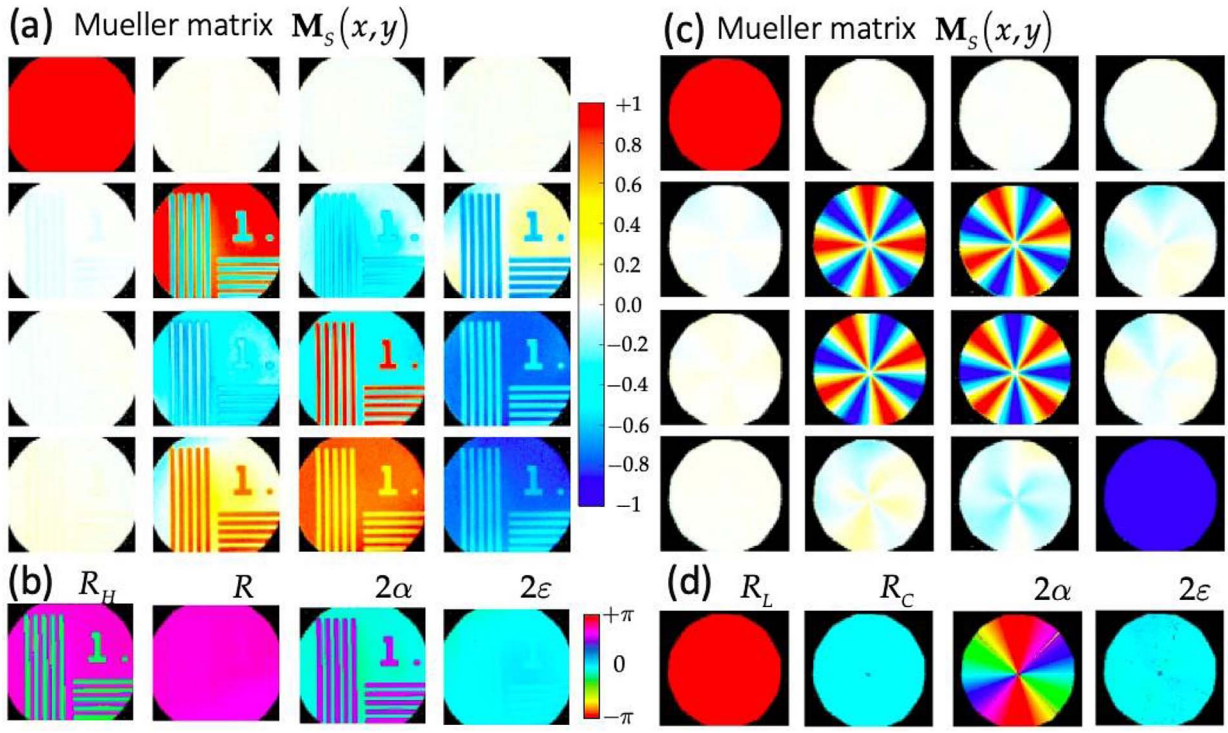

Fig. 6. (a) Experimental MM of the birefringent resolution test under red light channel illumination. (b) Retrieved horizontal linear retardance (R_L) and total retardance (R), and azimuth (α) and ellipticity (ε) of fast eigenstates. (c) and (d) show equivalent results for the q-plate element under red channel illumination.

and a pure depolarizer. These samples of well-defined properties thus serve as validation tests to probe the accuracy of the imaging polarimeter. For each sample, the experimental MM was retrieved following equation (9) and the Lu–Chipman decomposition $\mathbf{M}_S = \mathbf{M}_\Delta \cdot \mathbf{M}_R \cdot \mathbf{M}_D$ [37] was applied to calculate relevant polarimetric parameters using standard formulas [21]. We applied the very well-known Lu–Chipman decomposition because these samples, each of distinct physical mechanism, imply relatively simple Mueller matrices. Note that more complex Mueller matrices, simultaneously dealing with retardance, depolarization and diattenuation responses could require other decompositions, like for instance the inverse decomposition, the arrow form decomposition or the symmetric decomposition, among others [38].

As a first example, Figure 6 shows the results for two patterned retarders: a birefringent NBS 1963A resolution test (Thorlabs R2L2S1B), and a q-plate device (Thorlabs WPV10-633), both under the red channel illumination. Figures 6a and 6c show the retrieved MM normalized to m_{00}. They show the expected result for a retarder, where $m_{0j} = m_{j0} \approx 0$, for $j = 1, 2, 3$, indicating null polarizance and null diattenuation. The retarder information is contained in the 3×3 bottom right submatrix. The retardance vector [21, 37] is calculated and some representative parameters of the retarder are shown in each case.

Figures 6a and 6b show the results for the birefringent resolution test. This is a linear retarder designed to have a uniform retardance but a different orientation in the patterns compared to the background. The total retardance $R(x, y)$ appears uniform all over the image, with average value $\langle R \rangle = 131° \pm 1°$ (the value is obtained by averaging over the significant pixels and the error is given by its standard deviation, where again, the significant pixels are those comprised within a circle as defined in Fig. 3c). However, the horizontal component of the retardance vector $R_H(x, y)$ clearly shows a difference between the patterns and the background. The azimuth $\alpha(x, y)$ of the fast eigenstate confirms the two regions, with the background oriented approximately horizontal, $\langle \alpha_b \rangle = -8.5° \pm 0.5°$, and the resolution test pattern oriented at $\langle \alpha_t \rangle = -55.8° \pm 1.0°$. The ellipticity image $\varepsilon(x, y)$ of the fast eigenstate remains uniform over the entire image, with a very small value, $\langle \varepsilon \rangle = 2.6° \pm 1.2°$ as expected for a linear retarder.

Figures 6c and 6d show equivalent results for the q-plate component, a patterned retarder widely used to generate orbital angular momentum (OAM) beams and vector beams [39]. This is a linear retarder with fixed retardance and whose axes orientation changes azimuthally. This q-plate was designed as a half-wave retarder for the 633 nm wavelength and with value $q = 1$, so the retarder axes make a complete azimuthal rotation. In this case, since the retarder is very close to the half-wave condition, the most relevant information in the MM is in the m_{11}, m_{12}, m_{21}, and m_{22} elements, which show an azimuthal variation in the complete range from -1 to $+1$, and in the m_{33} element, which

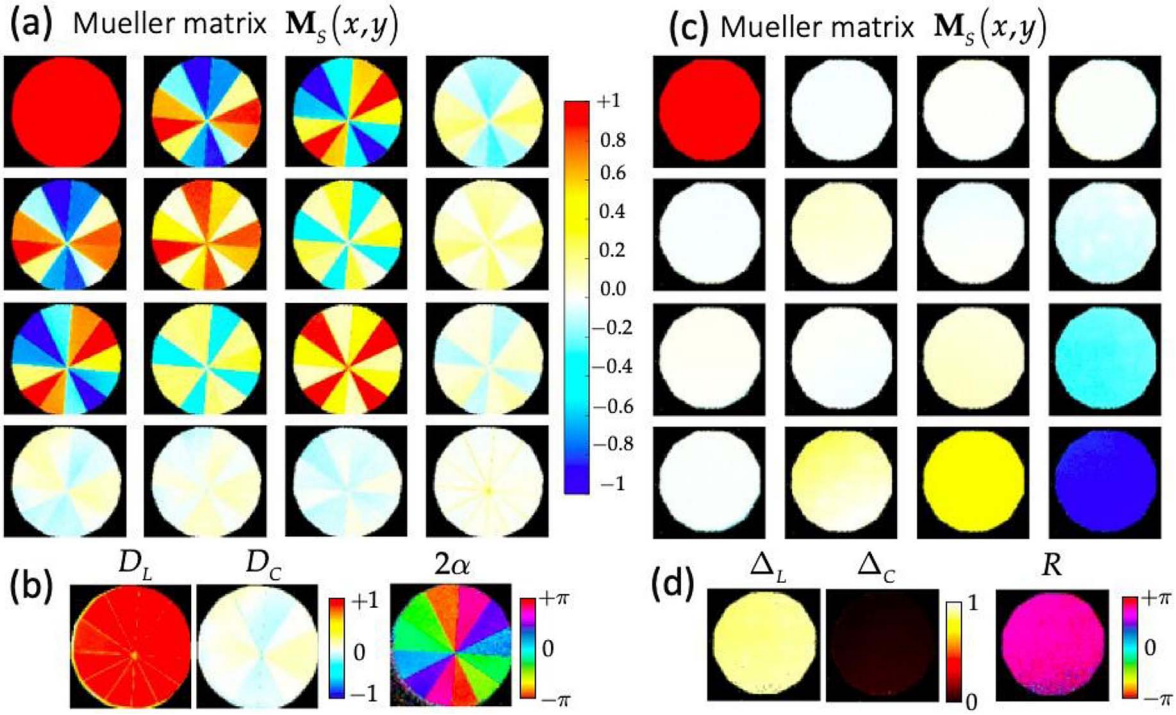

Fig. 7. (a) Experimental MM of a radial polarizer under red channel illumination. (b) Linear diattenuation (D_L), circular diattenuation (D_C), and azimuth (α) of the transmission axis. (c) Experimental MM for a depolarizing FLC modulator under the green channel illumination. (d) Linear depolarizance (Δ_L), circular depolarizance (Δ_C), and total effective retardance (R).

appears uniform with a value around −1. In this case Figure 6d illustrates the linear R_L and circular R_C components of the retardance vector, which confirm the linear retarder condition of this component. The total retardance is uniform with an average value $\langle R \rangle = 178° \pm 1.1°$ in agreement with the half-wave retardance design of this q-plate for red light. The azimuth of the fast eigenstate orientation $\alpha(x, y)$ shows a continuous azimuthal variation, as corresponding to a q-plate with $q = 1$ and the eigenstate ellipticity $\varepsilon(x, y)$ shows a null constant value with an average value $\langle \varepsilon \rangle = 1° \pm 3°$, as expected for a linear retarder.

The second type of structured polarization sample is a pure diattenuator: a radial polarizer from the company Codixx (ColorPol VIS500 BC3), consisting of 12 segments where the transmission axis is aligned radially, thus being shifted 30° between adjacent segments. Figure 7a shows the corresponding MM, again using the red channel. In this case the last row and column become null, $m_{3j} = m_{j3} \approx 0$ with $j = 0, 1, 2$. The other MM elements clearly show the segmentation of the polarizer. Figure 7b shows as parameters of interest the linear and circular components of the diattenuation, $D_L(x, y)$ and $D_C(x, y)$. The average total diattenuation is $\langle D \rangle = 0.85 \pm 0.13$, where again the value is averaged over the significant pixels and the error is given by its standard deviation. We also calculate the polarizer transmission angle $\alpha(x, y)$, which confirms the expected rotation.

Finally, as a pure depolarizing sample we consider a ferroelectric liquid–crystal (FLC) modulator. This type of modulator behaves as a linear retarder whose director axis switches between two stable orientations within the modulator plane [40]. When operated at a high frequency compared to the detector integration time, FLC modulators have proven to be useful to generate an effective depolarization [41]. In this work, we use a FLC modulator (CRL Opto LCS2-G) showing a switching angle of 45° and a retardance of 180° for green light [40]. We operate the device at a switching frequency of 500 Hz, much higher than the frame rate of the polarization camera. Therefore, each measurement with the camera corresponds to the incoherent superposition of the two states emerging from the FLC [42]. The measured MM can be regarded as the average of $\mathbf{M}_\mathrm{A}$ and $\mathbf{M}_\mathrm{B}$ the two matrices corresponding to the two stable states of the modulator.

The MM of a retarder with retardance φ and orientation α, corresponding to the first FLC stable position is given by [1]:

$$\mathbf{M}_\mathrm{A} = \begin{pmatrix} 1 & 0 & 0 & 0 \\ 0 & c_{2\alpha}^2 + c_\varphi s_{2\alpha}^2 & (1 - c_\varphi) s_{2\alpha} c_{2\alpha} & -s_\varphi s_{2\alpha} \\ 0 & (1 - c_\varphi) s_{2\alpha} c_{2\alpha} & s_{2\alpha}^2 + c_\varphi c_{2\alpha}^2 & s_\varphi c_{2\alpha} \\ 0 & s_\varphi s_{2\alpha} & -s_\varphi c_{2\alpha} & c_\varphi \end{pmatrix}, \tag{10}$$

where $c_x = \cos(x)$ and $s_x = \sin(x)$. The second FLC stable position is given by $\mathbf{M}_B = (-45°) \cdot \mathbf{M}_A \cdot \mathbf{R}(+45°)$ where $\mathbf{R}$ stands for the Mueller rotation matrix. Then, the average MM given by $\langle \mathbf{M}_\mathrm{FLC} \rangle = \frac{1}{2}(\mathbf{M}_A + \mathbf{M}_B)$ results in

$$\langle \mathbf{M}_{\mathrm{FLC}} \rangle = \begin{bmatrix} 1 & 0 & 0 & 0 \\ 0 & c_{2\varphi}^2 & 0 & -\frac{1}{2} s_\varphi (c_{2\alpha} + s_{2\alpha}) \\ 0 & 0 & c_{2\varphi}^2 & \frac{1}{2} s_\varphi (c_{2\alpha} + s_{2\alpha}) \\ 0 & \frac{1}{2} s_\varphi (c_{2\alpha} + s_{2\alpha}) & -\frac{1}{2} s_\varphi (c_{2\alpha} + s_{2\alpha}) & c_\varphi \end{bmatrix}. \tag{11}$$

In the case of a half-wave retardance, $\varphi = 180°$, this average matrix $\langle \mathbf{M}_{\mathrm{FLC}} \rangle$ becomes:

$$\langle \mathbf{M}_{\mathrm{FLC}} \rangle = \begin{pmatrix} 1 & 0 & 0 & 0 \\ 0 & 0 & 0 & 0 \\ 0 & 0 & 0 & 0 \\ 0 & 0 & 0 & -1 \end{pmatrix}. \tag{12}$$

This result can be regarded as a perfect depolarizer for input linear polarizations, whereas circular polarizations retain the full degree of polarization but change handedness.

Figure 7c shows the experimental MM results obtained with the polarimeter. In this case we use the green channel where the FLC layer behaves closely to the half-wave retardance condition [40]. Now the experimental MM elements are uniform images since the FLC modulator is a single-pixel element. The retrieved MM matches quite well the expected ideal result in equation (12). All the elements are close to zero, except $m_{00} \approx 1$ and $m_{33} \approx -1$. Elements m_{32} and m_{23} slightly differ from zero, due to the nonperfect half-wave retardance of the FLC layer. Figure 7d shows images of the depolarization and retardance parameters are calculated. The linear depolarizance $\Delta_L(x, y)$ shows high values, with an average value $\langle \Delta_L \rangle = 0.88 \pm 0.03$, while the circular depolarization $\Delta_C(x, y)$ has very low values, with $\langle \Delta_C \rangle = 0.04 \pm 0.03$. This confirms the ability of the FLC modulator to depolarize linearly polarized input light. Finally, the effective retardance $R(x, y)$ shows an average value $\langle R \rangle = 158° \pm 3°$, not far but non-perfect half-wave retardance. Again, the error given in these average values is calculated as the standard deviation of the values in all pixels in the aperture.

5 Conclusion

In summary, this work presents an imaging complete MM polarimeter comprised of a polarization camera and three LCRs. The use of polarization cameras in imaging systems is quite recent and it is arising high interest in a wide range of applications. The presented polarimeter is an improved version of our previous system [21] with significant advances. First, a multiwavelength LED light source replaced the laser source, thus avoiding interference and speckle derived from the coherent source. A rotatable breadboard is added to allow changing from the transmission configuration to a configuration useful for reflective or back-scattering samples. The system incorporates two LCRs in the PSG and another one in the PSA, to allow fully automated measurements without any moving element. All LCR devices were calibrated for the three spectral bands of the LED source.

The polarimeter was calibrated and compensated by modifying the time sequential method [25, 32]. The procedure has been illustrated step by step. The novelty here is that the polarization camera included in the polarimeter is itself the calibration reference. This way no additional external elements are required and the polarimeter can be fully optimized in situ. Furthermore, the procedure is applied at pixel level, therefore compensating the residual non-uniformities in the illumination and in the PSA system, because of the pixelwise calculation of the normalized Mueller matrix.

This approach of course relies on the quality of the polarization camera. To this aim, the Appendix incorporates a calculation of the error in the measurement of the MM elements caused by the limited extinction ratio (ER) of the micro-polarizers, which shows an error lower than 1.7% for the minimum value of ER = 120 measured in our camera. The calibration and compensation procedure has been illustrated step by step by displaying the $\mathbf{S}(x, y)$ and $\mathbf{A}(x, y)$ images that define the PSG and the PSA. They are compared with the theoretical expected values, showing a very good agreement in all cases.

Finally, three different samples used in structured light applications with well-known polarization properties were evaluated to verify the accuracy of the polarimeter: (1) two patterned pure retarders with constant retardance but different orientation of the optical axis (a birefringent resolution test and a q-plate), (2) a radial linear polarizer, and 3) a linear depolarizer based on a fast-switching FLC modulator with 45° switching angle. The retrieved experimental MM agree very well with the expected results and, after performing the Lu–Chipman decomposition, the polarization parameters of interest (retardance, diattenuation and depolarization) were derived in each case.

Funding

This work was financed by Ministerio de Ciencia e Innovación, Spain (refs.: PID2021-126509OB-C22, -C21 and PDC2022-133332-C22) and Generalitat Valenciana (ref. CIAICO/2021/276). EN acknowledges Generalitat Valenciana (ref. GRISOLIAP/2020/004). AV acknowledges Fondecyt N° 1191811.

Conflicts of Interest

This work has no financial or non-financial competing interests.

Data availability statement

Data will be made available on request.

Author contribution statement

All coauthors contributed to the paper. EN and AV contributed with the realization of the experiments. EN and IM contributed with the computer calculations. MMSL, AL, JC and IM contributed to the conceptualization, design of the experiments, and analysis of the results. MMSL contributed to writing the manuscript, and all authors contributed to the revision of the manuscript.

References

1 Goldstein D.H. (2010) *Polarized Light*, Marcel Dekker, New York, NY, USA.

2 Ramella-Roman J.C., Saytashev I., Piccini M. (2020) A review of polarization-based imaging technologies for clinical and preclinical applications, *J. Opt.* **22**, 123001. https://doi.org/10.1088/2040-8986/abbf8a.

3 He C., He H., Chang J., Chen B., Ma H., Booth M.J. (2021) Polarisation optics for biomedical and clinical applications: a review, *Light: Sci Appl.* **10**, 194. https://doi.org/10.1038/s41377-021-00639-x.

4 Gottlieb D., Arteaga O. (2021) Mueller matrix imaging with a polarization camera: application to microscopy, *Opt. Express* **29**, 21, 34723–34374. https://doi.org/10.1364/OE.439529.

5 Van Eeckhout A., Garcia-Caurel E., Garnatje T., Escalera J.C., Durfort M., Vidal J., Gil J.J., Campos J., Lizana A. (2021) Polarimetric imaging microscopy for advanced inspection of vegetal tissues, *Sci. Rep.* **11**, 3913. https://doi.org/10.1038/s41598-021-83421-8.

6 Rubinsztein-Dunlop H., Forbes A., Berry M.V., Dennis M.R., Andrews D.L., Mansuripur M., Denz C., Alpmann C., Banzer P., Bauer T., Karimi E., Marrucci L., Padgett M., Ritsch-Marte M., Litchinitser N.M., Bigelow N.P., Rosales-Guzmán C., Belmonte A., Torres J.P., Neely T.W., Baker M., Gordon R., Stilgoe A.B., Romero J., White A.G., Fickler R., Willner A.E., Xie G., McMorran B., Weiner A.M. (2017) Roadmap on structured light, *J. Opt.* **19**, 013001. https://doi.org/10.1088/2040-8978/19/1/013001.

7 Piquero G., Martínez-Herrero R., de Sande J.C.G., Santarsiero M. (2020) Synthesis and characterization of non-uniformly totally polarized light beams: tutorial, *J. Opt. Soc. Am. A* **37**, 4, 591. https://doi.org/10.1364/JOSAA.379439.

8 Rosales-Guzmán C., Ndagano B., Forbes A. (2018) A review of complex vector light fields and their applications, *J. Opt.* **20**, 123001. https://doi.org/10.1088/2040-8986/aaeb7d.

9 Devrinkas R., Kazansky P.G. (2017) High-performance geometric phase elements in silica glass, *APL Photon.* **2**, 066104. https://doi.org/10.1063/1.4984066.

10 Liu G.-G., Lee Y.-H., Huang Y., Zhu Z., Tan G., Cai M.-Q., Li P.-P., Wang D., Li Y., Pang S., Tu C., Wu S.-T., Wang H.-T. (2017) Dielectric broadband meta-vector-polarizers based on nematic liquid crystal, *APL Photon.* **2**, 066104. https://doi.org/10.1063/1.5006016.

11 Davis J.A., McNamara D.E., Cottrell D.M., Sonehara T. (2000) Two-dimensional polarization encoding with a phase-only liquid-crystal spatial light modulator, *Appl. Opt.* **39**, 10, 1549–1554. https://doi.org/10.1364/AO.39.001549.

12 Kenny F., Lara D., Rodríguez-Herrera O.G., Dainty C. (2012) Complete polarization and phase control for focus-shaping in high-NA microscopy, *Opt. Exp.* **20**, 13, 14015–14029. https://doi.org/10.1364/OE.20.014015.

13 Wen D., Croizier K.B. (2021) Metasurfaces 2.0: Laser-integrated and with vector field control, *APL Photon.* **6**, 080902. https://doi.org/10.1063/5.0057904.

14 De Sio L., Roberts D.E., Liao Z., Nersisyan S., Uskova O., Wickboldt L., Tabiryan N., Steeves D.M., Kimball B.R. (2016) Digital polarization holography advancing geometrical phase optics, *Opt. Exp.* **24**, 16, 18297–18306. https://doi.org/10.1364/OE.24.018297.

15 Curcio V., Alemán-Castañeda L.A., Brown T.G., Brasselet S., Alonso M.A. (2020) Birefringent Fourier filtering for single molecule coordinate and height super-resolution imaging with dithering and orientation, *Nature Commun.* **11**, 5307. https://doi.org/10.1038/s41467-020-19064-6.

16 Zhang Z., Dong F., Cheng T., Qiu K., Zhang Q., Chu W., Wu X. (2014) Nano-fabricated pixelated micropolarizer array for visible imaging polarimetry, *Rev. Sci. Instrum.* **85**, 105002. https://doi.org/10.1063/1.4897270.

17 Singh K., Tabebordbar N., Forbes A., Dudley A. (2020) Digital Stokes polarimetry and its application to structured light: tutorial, *J. Opt. Soc. Am. A* **37**, C33–C44. https://doi.org/10.1364/JOSAA.397912.

18 Angelo J.P., Germer T.A., Litorja M. (2019) Structured illumination Mueller matrix imaging, *Biomed. Opt. Exp.* **10**, 6, 2861–2868. https://doi.org/10.1364/BOE.10.002861.

19 Rubin N.A., D'Aversa G., Chevalier P., Shi Z., Chen W.T., Capasso F. (2019) Matrix Fourier optics enables a compact full-Stokes polarization camera, *Science* **365**, eaax1839. https://doi.org/10.1126/science.aax18.

20 Arteaga O., Bendada H. (2020) Geometrical phase optical components: Measuring geometric phase without interferometry, *Crystals* **10**, 880. https://doi.org/10.3390/cryst10100880.

21 López-Morales G., Sánchez-López M.M., Lizana A., Moreno I., Campos J. (2020) Mueller matrix polarimetric imaging analysis of optical components for the generation of cylindrical vector beams, *Crystals* **10**, 1155. https://doi.org/10.3390/cryst10121155.

22 Pezzaniti J.L., Chipman R.A. (1995) Mueller matrix imaging polarimetry, *Opt. Eng.* **34**, 6, 1558–1568. https://doi.org/10.1117/12.206161.

23 Kudenov M.W., Escuti M.J., Hagen N., Dereniak E.L., Oka K. (2012) Snapshot imaging Mueller matrix polarimeter using polarization gratings, *Opt. Lett.* **37**, 8, 1367–1369. https://doi.org/10.1364/OL.37.001367.

24 Carnicer A., Bosch S., Javidi B. (2019) Mueller matrix polarimetry with 3D integral imaging, *Opt. Exp.* **27**, 8, 11525–11536. https://doi.org/10.1364/OE.27.011525.

25 Garcia-Caurel E., Ossikovski R., Foldyna M., Pierangelo A., Drévillon B., De Martino A. (2013) Advanced Mueller ellipsometry instrumentation and data analysis (Chapter 2), in *Ellipsometry at the nanoscale*, M. Losurdo, K. Hingerl (eds.), Springer Verlag, Berlin.

26 Vargas A., Donoso R., Ramírez M., Carrión J., Sánchez-López M.M., Moreno I. (2013) Liquid crystal retarder spectral retardance characterization based on a Cauchy dispersion relation and a voltage transfer function, *Opt. Rev.* **20**, 5, 378–384. https://doi.org/10.1007/s10043-013-0068-4.

27 Messaadi A., Sánchez-López M.M., García-Martínez P., Vargas A., Moreno I. (2016) Optical system for measuring the spectral retardance function in an extended range, *J. Eur. Opt. Soc. – Rapid Pub.* **12**, 12, 21. https://doi.org/10.1186/s41476-016-0023-7.

28 Vargas A., Sánchez-López M.M., García-Martínez P., Arias J., Moreno I. (2014) Highly accurate spectral retardance characterization of a liquid crystal retarder including Fabry-Perot interference effects, *J. Appl. Phys.* **115**, 3, 033101. https://doi.org/10.1063/1.4861635.

29 Chipman R.A. (1995) Polarimetry, in *Handbook of Optics*, 2nd edn., McGraw-Hill, New York.

30 Twietmeyer K.M., Chipman R.A. (2008) Optimization of Mueller matrix polarimeters in the presence of error sources, *Opt. Exp.* **16**, 15, 11589–11603. https://doi.org/10.1364/OE.16.011589.

31 Peña-Gutiérrez S., Royo S. (2023) Polarization calibration assessment for a broadband imaging polarimeter based on a division of aperture architecture, *Opt. Exp.* **31**, 3, 3839–3856. https://doi.org/10.1364/OE.472070.

32 Peinado A., Lizana A., Vidal J., Iemmi C., Campos J. (2010) Optimization and performance criteria of a Stokes polarimeter based on two variable retarders, *Opt. Exp.* **18**, 8, 9815. https://doi.org/10.1364/OE.18.009815.

33 Cofré A., Vargas A., Torres-Ruiz F.A., Campos J., Lizana A., Sánchez-López M.M., Moreno I. (2017) Quantitative performance of a polarization diffraction grating polarimeter encoded onto two liquid-crystal-on-silicon displays, *Opt. Laser Technol.* **96**, 219–226. https://doi.org/10.1016/j.optlastec.2017.05.027.

34 Roussel S., Boffety M., Goudail F. (2018) Polarimetric precision of micropolarizer grid-based camera in the presence of additive and

Poisson shot noise, *Opt. Exp.* **26**, 23, 29968–29982. https://doi.org/10.1364/OE.26.029968.
35 Janesick J. (1997) CCD transfer method – standard for absolute performance of CCDs and digital CCD camera systems, *Proc. SPIE* **3019**, 70–102. https://doi.org/10.1117/12.275190.
36 Roussel S., Boffety M., Goudail F. (2019) On the optimal ways to perform full Stokes measurements with a linear division-of-focal plane polarimetric imager and a retarder, *Opt. Lett.* **44**, 11, 2927–2930. https://doi.org/10.1364/OL.44.002927.
37 Lu S.-Y., Chipman R.A. (1996) Interpretation of Mueller matrices based on polar decomposition, *J. Opt. Soc. Am. A* **13**, 5, 1106–1113. https://doi.org/10.1364/JOSAA.13.001106.
38 Gil J.J., Ossikovski R. (2022) *Polarized light and the mueller matrix approach*, CRC Press, New York. https://doi.org/10.1201/9780367815578.
39 Rubano A., Cardano F., Piccirillo B., Marrucci L. (2019) Q-plate technology: A progress review, *J. Opt. Soc. Am. B* **36**, 5, D70–D87. https://doi.org/10.1364/JOSAB.36.000D70.
40 Martínez A., Beaudoin N., Moreno I., Sánchez-López M.M., Velásquez P. (2006) Optimization of the contrast ratio of a ferroelectric liquid crystal optical modulator, *J. Opt. A: Pure Appl. Opt.* **8**, 11, 1013–1018. https://doi.org/10.1088/1464-4258/8/11/013.
41 Lizana A., Estévez I., Torres-Ruiz F.A., Peinado A., Ramirez C., Campos J. (2015) Arbitrary state of polarization with customized degree of polarization generator, *Opt. Lett.* **40**, 16, 3790–3793. https://doi.org/10.1364/OL.40.003790.
42 Marco D., López-Morales G., Sánchez-López M.M., Lizana A., Moreno I., Campos J. (2021) Customized depolarization spatial patterns with dynamic retardance functions, *Sci. Rep.* **11**, 9415. https://doi.org/10.1038/s41598-021-88515-x.

Appendix

A1 Evaluation of the micro-polarizers limited extinction ratio

The polarization camera has wire-grid micro-polarizers attached to the pixels of the CMOS detector. In this appendix we evaluate the accuracy of the polarimeter self-calibration procedure in terms of their extinction ratio. Since the polarization camera is used as the reference, the accuracy of the polarimeter calibration is dictated by the quality of its polarizers. Although other sources of errors have been identified (such as the spatial variation of the extinction ratio, or spatial variations in the orientation angle of the micro-polarizers transmission axes) [34], here we assume a simplified model where we consider the micro-polarizers perfectly oriented (horizontal, vertical, diagonal and antidiagonal), but having a limited and spatially uniform extinction ratio $\mathrm{ER} = T_{||}/T_{\perp}$ where $T_{||}$ and $T_{\perp}$ are the transmission for parallel and crossed polarizers respectively. Information about this main source of error in the polarization camera is provided by the supplier, indicating in our case values ER > 120:1 in the three colour bands. To take this into account, the MM of these four linear polarizers with limited ER is calculated analytically. The MM of a polarizer aligned horizontal and with limited extinction ratio is given by [1]:

$$\mathbf{P}_0 = \frac{T_{\|}}{2}\begin{pmatrix} 1+e & 1-e & 0 & 0 \\ 1-e & 1+e & 0 & 0 \\ 0 & 0 & 2\sqrt{e} & 0 \\ 0 & 0 & 0 & 2\sqrt{e} \end{pmatrix}, \tag{A1a}$$

where $e \equiv 1/\mathrm{ER} = T_{\perp}/T_{\|}$. The limit $e \to 0$ leads to the ideal polarizer with normalized MM:

$$\mathbf{P}_0(e=0) = \frac{T_{\|}}{2}\begin{pmatrix} 1 & 1 & 0 & 0 \\ 1 & 1 & 0 & 0 \\ 0 & 0 & 0 & 0 \\ 0 & 0 & 0 & 0 \end{pmatrix}. \tag{A1b}$$

We measured values ER > 120:1 for our camera polarizers in the three spectral bands, in agreement with the manufacturer data. The MM of the micro-polarizers oriented vertical and at ±45° are simply obtained by applying the corresponding rotation transformation [1].

Assuming ideal input states (ideal values in the **S** matrix in Eq. (3)), and that the circular components R and L are measured using an ideal QWP in front of the camera, the intensity measured for each input state when being analyzed with these limited linear micro-polarizers can be calculated analytically, leading to an intensity matrix as in equation (5) which now takes the following form:

See the equation (A2) bottom of the page

where the ideal matrix in equation (5) is recovered for the limit $e \to 0$ and $T_{\|} \to 1$. Hence, equation (A2) is the intensity matrix of the polarimeter calibration, which contains the errors induced by the limited ER of the micro-polarizers. The analytical expression of the calibrated PSA matrix that compensates the limited ER is thus obtained as $\mathbf{A}(e) = \mathbf{I}_{\mathrm{air}}(e) \cdot \mathbf{S}^{-1}$) using equation (A2) and the ideal $\mathbf{S}^{-1}$ matrix in equation (4). Its pseudo-inverse is given by:

$$\mathbf{A}^{-1}(e) = \frac{1}{T_{\|}}\begin{pmatrix} \frac{1}{3(1+e)} & \frac{1}{3(1+e)} & \frac{1}{3(1+e)} & \frac{1}{3(1+e)} & \frac{1}{3(1+e)} & \frac{1}{3(1+e)} \\ \frac{1}{1-e} & \frac{1}{1-e} & 0 & 0 & 0 & 0 \\ 0 & 0 & \frac{1}{1-e} & \frac{1}{1-e} & 0 & 0 \\ 0 & 0 & 0 & 0 & \frac{1}{1-e} & \frac{1}{1-e} \end{pmatrix}. \tag{A3}$$

$$\mathbf{I}_{\mathrm{air}}(e) = T_{\|}\begin{pmatrix} 1 & e & \frac{1}{2}(1+e) & \frac{1}{2}(1+e) & \frac{1}{2}(1+e) & \frac{1}{2}(1+e) \\ e & 1 & \frac{1}{2}(1+e) & \frac{1}{2}(1+e) & \frac{1}{2}(1+e) & \frac{1}{2}(1+e) \\ \frac{1}{2}(1+e) & \frac{1}{2}(1+e) & 1 & e & \frac{1}{2}(1+e) & \frac{1}{2}(1+e) \\ \frac{1}{2}(1+e) & \frac{1}{2}(1+e) & e & 1 & \frac{1}{2}(1+e) & \frac{1}{2}(1+e) \\ \frac{1}{2}(1+e) & \frac{1}{2}(1+e) & \frac{1}{2}(1+e) & \frac{1}{2}(1+e) & 1 & e \\ \frac{1}{2}(1+e) & \frac{1}{2}(1+e) & \frac{1}{2}(1+e) & \frac{1}{2}(1+e) & e & 1 \end{pmatrix}, \tag{A2}$$

This matrix recovers the ideal case in the right part of equation (7) in the limit when $e \to 0$ and $T_{\parallel} \to 1$.

To evaluate analytically the impact of the limited extinction ratio on the polarimeter measurement, we first consider as sample the air and apply equation (9), $\mathbf{M} = \mathbf{A}^{-1}\,\mathbf{I}\,\mathbf{S}^{-1}$, to obtain the MM of air. Here we use the non-ideal intensity matrix $\mathbf{I}_{\text{air}}$ in equation (A2), but we consider the ideal values of the matrices $\mathbf{S}^{-1}$ and $\mathbf{A}^{-1}$ given in the right part of equation (4) and equation (7) respectively. This way we assume that the polarizers extinction ratio error is present in the experiment, but it is ignored in the polarimetric calculation. The analytical calculation leads to a MM matrix affected by the error e given by:

$$\mathbf{M}_{\text{air}}(e) = \mathbf{A}^{-1}\cdot\mathbf{I}_{\text{air}}(e)\cdot\mathbf{S}^{-1} = T_{\parallel}\begin{pmatrix} 1+e & 0 & 0 & 0 \\ 0 & 1-e & 0 & 0 \\ 0 & 0 & 1-e & 0 \\ 0 & 0 & 0 & 1-e \end{pmatrix}, \tag{A4}$$

which recovers the expected identity matrix of air when $e \to 0$ and $T_{\parallel} \to 1$. The MM in equation (A4) can be rewritten as

$$\mathbf{M}_{\text{air}}(e) = T_{\parallel}(1+e)\begin{pmatrix} 1 & 0 & 0 & 0 \\ 0 & 1-\delta & 0 & 0 \\ 0 & 0 & 1-\delta & 0 \\ 0 & 0 & 0 & 1-\delta \end{pmatrix}, \tag{A5}$$

which shows that the MM normalized to m_{00} has diagonal elements $m_{11} = m_{22} = m_{33} = (1-e)/(1+e) \equiv 1-\delta$. This result reflects that the limited extinction ratio of the camera micro-polarizers induces an error δ in the diagonal elements of the normalized MM for air given by:

$$\delta = 1 - \frac{1-e}{1+e} = \frac{2e}{1+e} = \frac{2}{1+ER} \simeq \frac{2}{ER}, \tag{A6}$$

where we used that $e = 1/ER$ and $ER \gg 1$ in the final approximation. Figure A1 shows the evolution of this error parameter as a function of the extinction ratio. Since ER $>$ 120:1 in our polarization camera, the deviation expected from this problem is $\delta < 1.7\%$.

Obviously, the identity MM of air is also recovered when the PSA calibration compensates for the limited ER i.e., when using the PSA pseudo-inverse matrix $\mathbf{A}^{-1}(e)$ in equation (A3). Then equation (9) results directly on the identity matrix since $\mathbf{A}^{-1}(e)\cdot\mathbf{I}_{\text{air}}(e)\cdot\mathbf{S}^{-1} = \mathbf{A}^{-1}(e)\cdot\mathbf{A}(e)$.

We can now analytically show that, for any other sample, the procedure described in Section 4 compensates the limited ER of the micro-polarizers if the PSA pseudo-inverse matrix $\mathbf{A}^{-1}(e)$ in equation (A3) is the one employed to retrieve the Mueller matrix. To illustrate this, we consider as sample an ideal linear polarizer with horizontal transmission axis, whose MM is given by equation (A1b). The 6 × 6 elements of the intensity matrix $\mathbf{I}_{\text{p}}(e)$ of this polarizer sample are analytically obtained by calculating the intensity I_{ag} expected for each input state, g = H, V, D, A, R, L (assumed ideal), when being detected through analyzers a = H, V, D, A, R, L affected by a limited extinction ratio ($e \neq 0$). In this case, the obtained intensity matrix is:

See the equation (A7) bottom of the page

The MM of this polarizer sample is then obtained from equation (9). If the calculation is made ignoring the error in the micro-polarizers, i.e., using the ideal $\mathbf{A}^{-1}$ matrix defined equation (7), the analytical expression of such non-compensated MM is:

$$\mathbf{M}_{p}(e) = \mathbf{A}^{-1}\cdot\mathbf{I}_{p}(e)\cdot\mathbf{S}^{-1} = \frac{T_{\parallel}}{2}(1+e)\begin{pmatrix} 1 & 1 & 0 & 0 \\ 1-\delta & 1-\delta & 0 & 0 \\ 0 & 0 & 0 & 0 \\ 0 & 0 & 0 & 0 \end{pmatrix}. \tag{A8}$$

Thus, the the normalized MM contains errors in the m_{10} and m_{11} elements. These errors are completely compensated by using the pseudo-inverse matrix $\mathbf{A}^{-1}(e)$ of equation (A3). A simple calculation shows that the matrix product $\mathbf{A}^{-1}(e)\ \mathbf{I}_{p}(e)\ \mathbf{S}^{-1}$ results in the expected MM in equation (A1b).

Finally, the same kind of calculation can be generalized to an arbitrary sample described by a generic MM:

$$\mathbf{M}_{s} = \begin{pmatrix} m_{00} & m_{01} & m_{02} & m_{03} \\ m_{10} & m_{11} & m_{12} & m_{13} \\ m_{20} & m_{21} & m_{22} & m_{23} \\ m_{30} & m_{31} & m_{32} & m_{33} \end{pmatrix}. \tag{A9}$$

We again evaluate analytically the intensity matrix $I_{\text{s}}(e)$ when the sample is introduced in the polarimeter affected by the error e. We calculate the intensity I_{ag} expected for each input state g = H, V, D, A, R, L (assumed ideal), when

$$I_{p}(e) = T_{\parallel}\begin{pmatrix} 1 & e & \frac{1}{2} & \frac{1}{2} & \frac{1}{2} & \frac{1}{2} \\ e & 1 & \frac{1}{2}e & \frac{1}{2}e & \frac{1}{2}e & \frac{1}{2}e \\ \frac{1}{2}(1+e) & 0 & \frac{1}{4}(1+e) & \frac{1}{4}(1+e) & \frac{1}{4}(1+e) & \frac{1}{4}(1+e) \\ \frac{1}{2}(1+e) & 0 & \frac{1}{4}(1+e) & \frac{1}{4}(1+e) & \frac{1}{4}(1+e) & \frac{1}{4}(1+e) \\ \frac{1}{2}(1+e) & 0 & \frac{1}{4}(1+e) & \frac{1}{4}(1+e) & \frac{1}{4}(1+e) & \frac{1}{4}(1+e) \\ \frac{1}{2}(1+e) & 0 & \frac{1}{4}(1+e) & \frac{1}{4}(1+e) & \frac{1}{4}(1+e) & \frac{1}{4}(1+e) \end{pmatrix} \tag{A7}$$

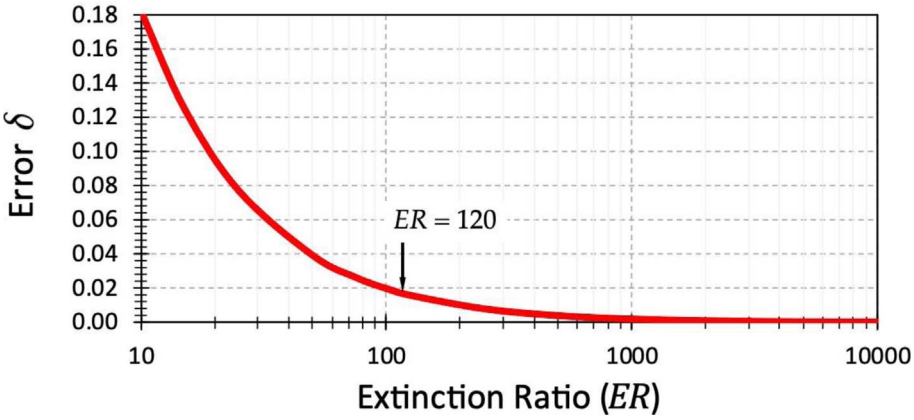

Fig. A1. Evolution of the error parameter δ as a function of the polarizers extinction ratio ER. The arrow indicates the limit value $ER = 120$ measured for our polarization camera.

$$M_s(e) = T_{\parallel}(1+e)\begin{pmatrix} m_{00} & m_{01} & m_{02} & m_{03} \\ m_{10}(1-\delta) & m_{11}(1-\delta) & m_{12}(1-\delta) & m_{13}(1-\delta) \\ m_{20}(1-\delta) & m_{21}(1-\delta) & m_{22}(1-\delta) & m_{23}(1-\delta) \\ m_{30}(1-\delta) & m_{31}(1-\delta) & m_{32}(1-\delta) & m_{33}(1-\delta) \end{pmatrix}, \tag{A10}$$

being detected through analyzers a = H, V, D, A, R, L affected by a limited extinction ratio ($e \neq 0$). Again, the impact of the limited extinction ratio on the polarimeter measurement can be analytically evaluated by considering equation (9), $\mathbf{M}_{\mathrm{S}}(e) = \mathbf{A}^{-1} \cdot \mathbf{I}_{\mathrm{S}}(e) \cdot \mathbf{S}^{-1}$, where the ideal $\mathbf{A}^{-1}$ is applied (thus ignoring the error in the micro-polarizers). It is a long but straightforward calculation to obtain that the retrieved MM reads:

See the equation (A10) top of the page

which recovers the ideal matrix in equation (A9) in the limit $e \to 0$ ($\delta \to 0$) and $T_{\parallel} \to 1$. This shows that all elements in the normalized MM except those in the first row are affected by the same factor $1 - \delta$.

However, it can also be demonstrated that the sample matrix in equation (A10) is recovered when using the PSA matrix in equation (A3) to calculate $\mathbf{A}^{-1}(e) \cdot \mathbf{I}_{\mathrm{s}}(e) \cdot \mathbf{S}^{-1} = \mathbf{M}_{\mathrm{s}}$, i.e., the ER error of the micro-polarizers is completely compensated.

Finally, let us note that we are applying this compensation method to a simplified model where only a uniform limited extinction ratio of the micro-polarizers is considered. The effect of spatial variations of the extinction ratio or errors in the orientation of the micro-polarizers can be considered as indicated in [34].